Prognostic Monitoring of Power QFN Packages With Silver Sintered Die-Attach Materials

Henry A. Martin, *Member, IEEE*, Dong Hu, *Member, IEEE*, Xu Liu, René H. Poelma, *Senior Member, IEEE*, Edsger C. P. Smits, Willem D. van Driel, and GuoQi Zhang, *Fellow, IEEE*

***Abstract*— Prognostic monitoring of power quad flat no-lead (PQFN) packages with four distinct silver pastes, each varying in material composition (pure-Ag and resin-reinforced hybrid-Ag) and sintering processes (pressure-assisted and pressureless), was investigated in this study. The PQFN packages with silver sintered die-attach materials were subjected to thermal cycling tests (−55 °C to 150 °C), and the performance degradation was evaluated based on the following metrics: 1) electrical ON-state resistance R_{DSon} monitored periodically at specific thermal cycling intervals and 2) transient thermal impedance $Z_{th}(t = 0.1\ s)$ monitored online during thermal cycling. These measurements were further validated using acoustic microscopy imaging and cross-sectional inspection. The pressureless Ag-sintering material demonstrated comparable performance to pressure-assisted Ag-sintering, with a dense microstructure, and consistent electrical and stable thermal performance. Whereas the pressureless resin-reinforced hybrid-Ag material exhibited degradation with a relative increase of ∼33% in R_{DSon}, ∼38% in $Z_{th}(t = 0.1\ s)$, and ∼67% delamination of the die-attach interface over 1000 cycles. These findings suggest that pressureless Ag-sintering may offer a viable alternative to pressure-assisted methods for lead (Pb)-free die-attachments, while resin-reinforced hybrid-Ag requires further development for improved thermomechanical reliability.**

***Index Terms*— Acoustic microscopy, condition monitoring, lead (Pb)-free die-attach, silver sintering, thermal cycling.**

TABLE I

STORAGE AND PROCESS CONDITIONS OF SILVER SINTER PASTES USED IN THIS STUDY. THE PROCESS CONDITIONS WERE CHOSEN BASED ON PRIOR EXPERIMENTAL ANALYSIS

	Material-A	Material-B	Material-C	Material-D
Type	Pressure Ag-Sintering	Pressure Ag-Sintering	Pressureless Ag-Sintering	Pressureless Resin-Reinforced Hybrid-Ag
Storage Conditions	∼ 10°C	−40°C	Room Temperature	−40°C
Pre-Conditioning	Thawing	Thawing	Thawing	Thawing
Pre-Drying Temperature	130°C	80°C	N/A	N/A
Pre-Drying Time	5 minutes	30 minutes	N/A	N/A
Sintering Pressure	20MPa	10MPa	N/A	N/A
Sintering Temperature	250°C	250°C	90°C & 250°C	200°C
Sintering Time	5 minutes	5 minutes	10 minutes & 45 minutes	90 minutes
Sintering Atmosphere	N_2 (or) Forming gas	N_2 (or) Forming gas	N_2 (or) Forming gas	N_2 (or) Forming gas

I. INTRODUCTION

RELIABILITY stands as a critical performance metric for sustainable packaging in electronics. However, meeting reliability requirements presents several challenges. These include catering to field-critical applications, enduring harsh environmental conditions, complying with rigorous testing and safety regulations, accommodating the demand for higher power density, managing complex integration processes, and navigating uncertainties due to new materials [1], [2], [3], [4].

The dominant degradation mechanism on electronic packages arises from temperature fluctuations and mismatched material properties, particularly die-attach layers subjected to thermomechanical loading conditions [5], [6]. Growing emphasis on the robustness of die-attach materials is challenged in meeting application-specific requisites. Restrictions on lead (Pb) solders and concerns over the environmental and health impacts of 1-methyl-2-pyrrolidone (NMP) and per-and-poly-fluoroalkyl substances (PFAS) regulate material suppliers to review the chemicals used in their die-attach adhesive manufacturing processes [7], [8].

Silver sintering technology offers a promising solution for Pb-free die-attachments in electronic packaging due to its low electrical resistivity (<2 $\mu\Omega$-cm) and heightened thermal conductivity (∼100–200 W/mK) [9], [10], [11], [12], [13], [14]. Additionally, silver sintering allows processing at relatively low temperatures (∼200 °C to 300 °C) while achieving a high melting point (∼900 °C to 1000 °C) after

Manuscript received 29 July 2024; accepted 11 August 2024. Date of publication 14 August 2024; date of current version 3 January 2025. This work was supported in part by Delft University of Technology and in part by the Chip Integration Technology Center. Recommended for publication by Associate Editor L. Codecasa upon evaluation of reviewers' comments. *(Corresponding author: Henry A. Martin.)*

Henry A. Martin is with the Electronics Components Technology and Materials Group, Delft University of Technology, 2628 CD Delft, The Netherlands, and also with the Chip Integration Technology Center, 6534 AT Nijmegen, The Netherlands (e-mail: henry.martin@citc.org).

Dong Hu and GuoQi Zhang are with the Electronics Components Technology and Materials Group, Delft University of Technology, 2628 CD Delft, The Netherlands (e-mail: d.hu@tudelft.nl; g.q.zhang@tudelft.nl).

Xu Liu and René H. Poelma are with the Electronics Components Technology and Materials Group, Delft University of Technology, 2628 CD Delft, The Netherlands, and also with Nexperia BV, 6534 AB Nijmegen, The Netherlands (e-mail: xu.liu@nexperia.com; rene.poelma@nexperia.com).

Edsger C. P. Smits is with the Chip Integration Technology Center, 6534 AT Nijmegen, The Netherlands (e-mail: edsger.smits@citc.org).

Willem D. van Driel is with the Electronics Components Technology and Materials Group, Delft University of Technology, 2628 CD Delft, The Netherlands, and also with Signify NV, 5656 AE Eindhoven, The Netherlands (e-mail: w.d.vandriel-1@tudelft.nl).

Color versions of one or more figures in this article are available at https://doi.org/10.1109/TCPMT.2024.3443530.

Digital Object Identifier 10.1109/TCPMT.2024.3443530

processing, reducing the risk of oxidation compared to copper sintering materials [15]. However, the formation of reliable sintered interconnects for both silver and copper pastes is influenced by several factors, including paste rheology (solvents and binders), particle composition (shape and size distribution), sintering process parameters (time, temperature, and pressure), process conditions (staging time, sintering method—convective or conductive, and ambient environment), and paste shelf life [16], [17], [18], [19], [20], [21]. Recently, hybrid silver materials gained increasing attention for their ability to sinter at even lower temperatures ($\leq$200 °C) and their relatively lower modulus [22], [23], [24], [25].

Several studies characterized the viscoplastic behavior and creep response of silver sintering materials [26], [27], [28], [29]. However, there is a notable gap in understanding the impact of different silver sintering materials and their processing conditions on the long-term reliability of functional electronic packages. This study addresses this gap by systematically evaluating packages with four distinct silver sintering materials (see Table I), varying in material composition (pure-Ag and resin-reinforced hybrid-Ag) and sintering process (pressure-assisted and pressureless). Accordingly, the package performance was evaluated based on the following methods.

1) Changes in electrical ON-state resistance R_{DSon} and transient thermal impedance $Z_{\mathrm{th}}(t = 0.1\ \mathrm{s})$ monitored during thermal cycling. R_{DSon} was measured intermittently using four-point kelvin contacts between the metal–oxide–semiconductor field effect transistor (MOSFET) source and drain (leadframe), while $Z_{\mathrm{th}}(t = 0.1\ \mathrm{s})$ was measured online by applying a brief localized transient heat pulse.
2) Degradation of packages imaged intermittently during thermal cycling using acoustic microscopy.
3) Cross-sectional inspection of the die-attach interface after 1000 thermal cycles.

Understanding the package performance degradation necessitates monitoring strategies to create better awareness of the component's health [30], [31], [32]. Monitoring the device R_{DSon} and $Z_{\mathrm{th}}(t)$ facilitates informed decisions regarding derating and preemptive maintenance. Section II covers the package assembly processes, with a concise overview of the experimental setup and monitoring parameters. The results are further presented with a brief discussion.

II. Experimental Methods

A. Sample Preparation

Silicon-based N-channel enhancement mode MOSFETs of 4.5 × 5.5 mm were used as a test vehicle. These MOSFETs are 170 μm thick and are commercially utilized in high-performance automotive systems. Silver sintering pastes specifically formulated for assemblies of large die on silver finish substrates were chosen in this study. The material type, storage, and processing conditions of the pastes are provided in Table I. The fundamental differences between all four material types are as follows.

1) Material-A contains >80% Ag particles dispersed in a solvent, with an average particle size of ~100 nm. During sintering at 250 °C and 20 MPa, the organics evaporate, resulting in a dense Ag-sintered interface (<10% porous) with a modulus expected to be closer to bulk Ag. Wereszczak et al. [33] correlate elastic modulus with sintered-Ag density.
2) Material-B contains ~75%–90% of Ag content with organic solvents. Upon sintering at 250 °C and 10 MPa pressure, the sintered interface is relatively dense with modulus expected to be lower than Material-A.
3) Material-C contains a high Ag concentration of ~90%–95%. Despite the pressureless sintering process at 250 °C, this material is expected to form a dense sintered interconnect with a relatively high elastic modulus due to rich Ag content.
4) Material-D is a hybrid-Ag sintering technology with ~80%–90% of Ag, ~1%–10% of resin to reinforce the porous interface, <5% additives, and ~5%–10% of high-boiling solvent. This hybrid-Ag material has a relatively lower modulus (~17 GPa).

It is important to be aware that the material composition mentioned above is in weight percentages. Also, the compounds and the expected modulus mentioned are based on the material datasheet.

In this study, the MOSFETs were assembled into a power quad flat no-lead (PQFN) surface mount, nonhermetically sealed package. The substrate is made of copper with Ag-metallization. The backside of the silicon MOSFETs was metalized with Ag to promote adhesion and reduce intermetallics. The silver pastes were preconditioned (thawed) to achieve consistency upon printing. An overview of the package assembly processes is provided in Fig. 1.

1) The silver pastes were stencil-printed over the die-pad of the leadframe. The MOSFETs were subsequently placed using a force-controlled die-bonder and sintered according to the prescribed process conditions in Table I. A schematic representation of the printed Ag-paste and sintered die is shown in Fig. 1(a).
   a) The pressure-assisted sintering process was carried out using a wafer bonder with minor adjustments for pressure sintering. The printed wet-paste first underwent a predrying stage (without die) according to the process parameters specified in Table I. Uniform pressure is applied over the leadframe under nitrogen (N_2) ambient [see Fig. 1(a_1)].
   b) The pressureless process was carried out using an industrial hot plate sintering oven under N_2 ambient [see Fig. 1(a_2)].
   c) The prescribed process conditions for both pressure-assisted and pressureless sintering were chosen from prior experimental analysis. It is important to be aware that the pressure sintering process adapted using a wafer bonder may not adequately represent the commercial pressure sintering tools, which are preheated to the sintering temperature.
2) Upon sintering, the assembled devices were wire-bonded with 25-μm-thick aluminum wires. All electrical

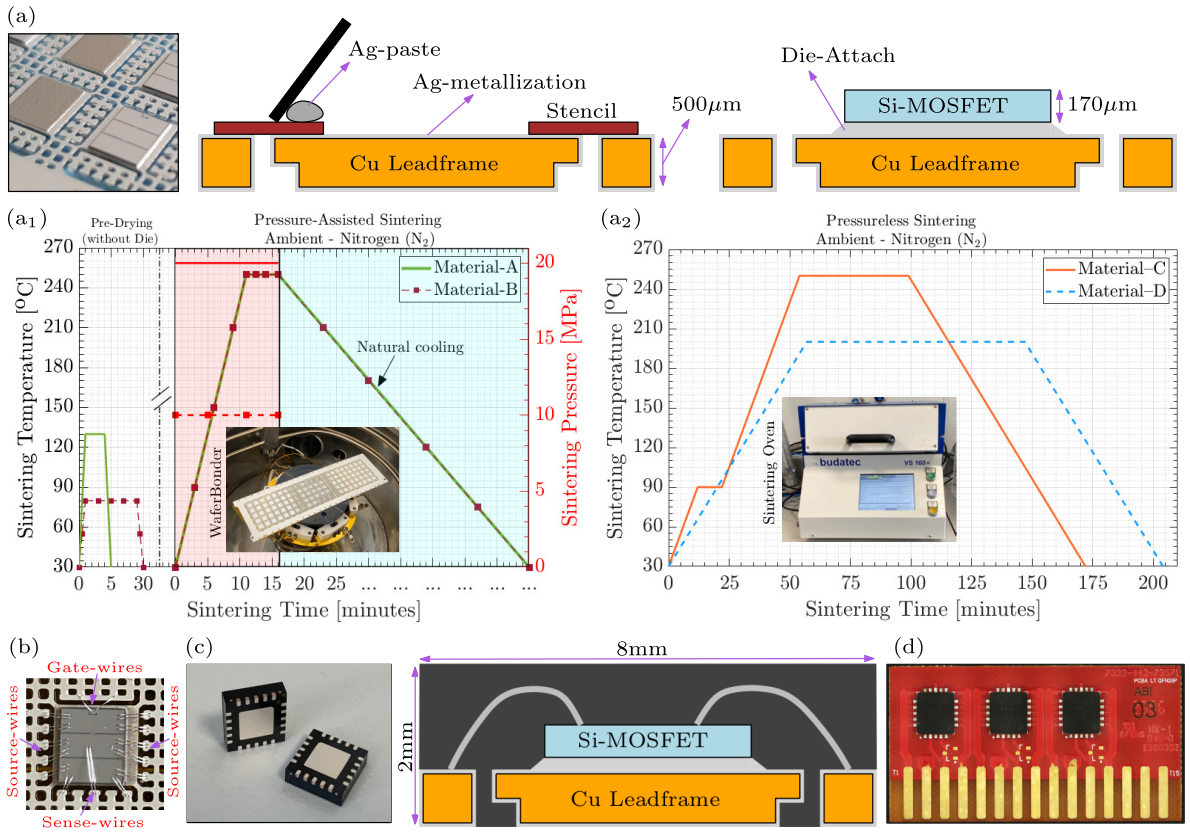

Fig. 1. (a) Stencil printing and sintering of the die to the leadframe. (a$_1$) Pressure-assisted sintering process. (a$_2$) Pressureless sintering process. (b) Electrical connections through wire bonds. (c) Encapsulated, singulated, and laser-marked PQFN packages. (d) Packages soldered to test boards.

connections are made of four-point kelvin contacts between the MOSFET source and the drain (die-pad) terminals [see Fig. 1(b)]. The gate terminal is connected separately. Four-point probe configuration enables precise monitoring of the device's ON-state resistance (R_{DSon}).

3) The samples are further encapsulated using a commercial epoxy molding compound at 175 °C. The molded samples are then singulated into separate PQFN packages and laser-marked for unique identification. A schematic of the packaged device is shown in Fig. 1(c).
4) Individual PQFN packages are further soldered using SAC305 onto a specially designed test board, which accommodates three packages with separate source and sense wires for four-point connections [see Fig. 1(d)].

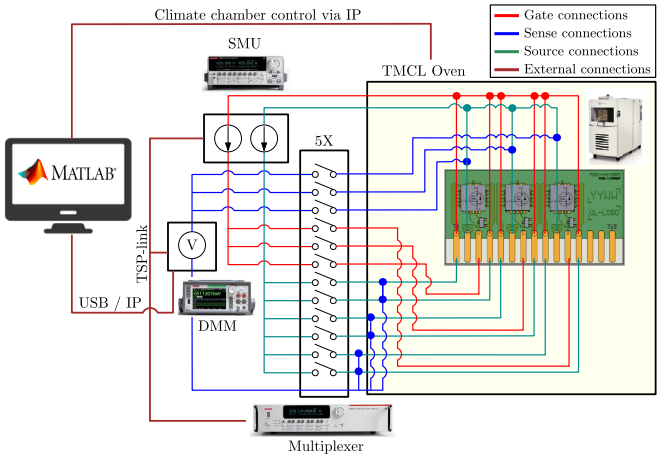

Fig. 2. Schematic illustration of the experimental setup with different connections color-coded.

B. Measurement Setup

A dedicated measurement setup was developed for monitoring the package performance during thermal cycling tests (see Fig. 2). The setup contains sockets for mounting test boards inside a thermomechanical cycling lifetime (TMCL) oven with electrical connections extending from the test socket to the sourcing and measuring equipment via a multiplexer (switch matrix). The multiplexer enables sequential measurements of multiple devices during testing conditions with a maximum switching current of 1 A (hot switching). A dual-channel source measurement unit (SMU) was used for sourcing drain current (I_D) and applying gate–source voltage (V_{GS}). A digital multimeter (DMM) was used for measuring the voltage across the drain–source terminals (V_{DS}). The polarity was reversed while measuring the body diode of the device.

C. Measurement Conditions and Monitoring Parameters

The lifetime reliability of PQFN packages with diverse sintering materials was evaluated under thermal cycling conditions. The cycling temperature ranged from −55 °C to 150 °C according to the stress test qualification for automotive discrete devices outlined in AECQ101 testing guidelines. The

JESD22-A104 thermal cycling standards were adapted with an additional measurement step at 25 °C during every cycle for online monitoring. The experimental temperature cycling profile used in this study is depicted in Fig. 3(a).

Two monitoring parameters were chosen to evaluate the package performance over cycling: 1) electrical ON-state resistance R_{DSon} under forward bias and 2) transient thermal impedance $Z_{\mathrm{th}}(t)$ under reverse bias.

Similar studies on reliability investigation based on electrical and thermal measurements were previously assessed under power cycling conditions [32], [34]. The MOSFET typically exhibits ON-state resistance (R_{DSon}) in the range of a few milliohms at room temperature (∼25 °C), and the measuring equipment has a resolution of 0.1 μV for voltages up to 1 V. The R_{DSon} was measured using four-point kelvin contacts, applying 10 V over the gate terminal and 1-A drain current over the drain–source terminals. No visible self-heating effects were observed over five seconds, and an average ON-state resistance (R_{DSon}-Avg) was determined [see Fig. 3(b)]. The R_{DSon}-Avg parameter denotes the resistance across the die (R_{Die}), the die-attach (R_{DA}), the leadframe (R_{LF}), the solder joint interface (R_S), and other contact resistances (R_C). The wire bond resistances (R_{Wire}) can be ignored due to four-point kelvin contacts between source and drain terminals

$$R_{\mathrm{DSon}} - \mathrm{Avg} \approx R_{\mathrm{Die}} + R_{\mathrm{DA}} + R_{\mathrm{LF}} + R_S + R_C. \quad (1)$$

Since the four-point measurements eliminate the influence of resistances from wire bonds and other printed circuit board (PCB) materials, the changes in the measured R_{DSon} must reflect alterations within the packaging components.

Measuring the transient thermal impedance $Z_{\mathrm{th}}(t)$ of a package involves localized heating and measuring the device temperature. The Si-MOSFET's intrinsic body diode exhibits a linear temperature sensitivity of ∼2.26 mV/ °C across the thermal cycling range [see Fig. 3(c)]. With 0 V applied over the gate terminal, the transistor channel remains closed, allowing source current ($I_S = -I_D$) to flowthrough the body diode. No changes in V_{SD} were observed upon applying negative gate–source voltages ($-V_{\mathrm{GS}}$). Varying the source current I_S allows localized heating and estimating the junction temperature.

Traditional thermal characterization methods outlined in MIL-STD-883E and JESD51-14 to determine the junction-to-case thermal resistance $Z_{\mathrm{th(j\text{-}c)}}(t)$ are not suitable for online monitoring during thermal cycling. The MIL-STD-883E requires steady-state temperature measurement over the junction and the case, while the JESD51-14 relies on relative comparison with and without thermal interface material. Besides, the JESD51-14 assumes a 1-D heat flow, thereby requiring a water-cooled heat sink to limit lateral heat spreading, which is not feasible for integration with thermal cycling. Hence, the transient thermal impedance $Z_{\mathrm{th}}(t)$ was determined based on a transient pulse [see Fig. 3(d)]. The measured $Z_{\mathrm{th}}(t = 0.1\ \mathrm{s})$ is not the same as $Z_{\mathrm{th(j\text{-}c)}}(t)$. A detailed explanation of extracting $Z_{\mathrm{th}}(t)$ from a transient pulse is provided in [30], and a review of measurement methods for thermal resistance extraction based on temperature sensitive electrical parameters (TSEP) is provided in [35].

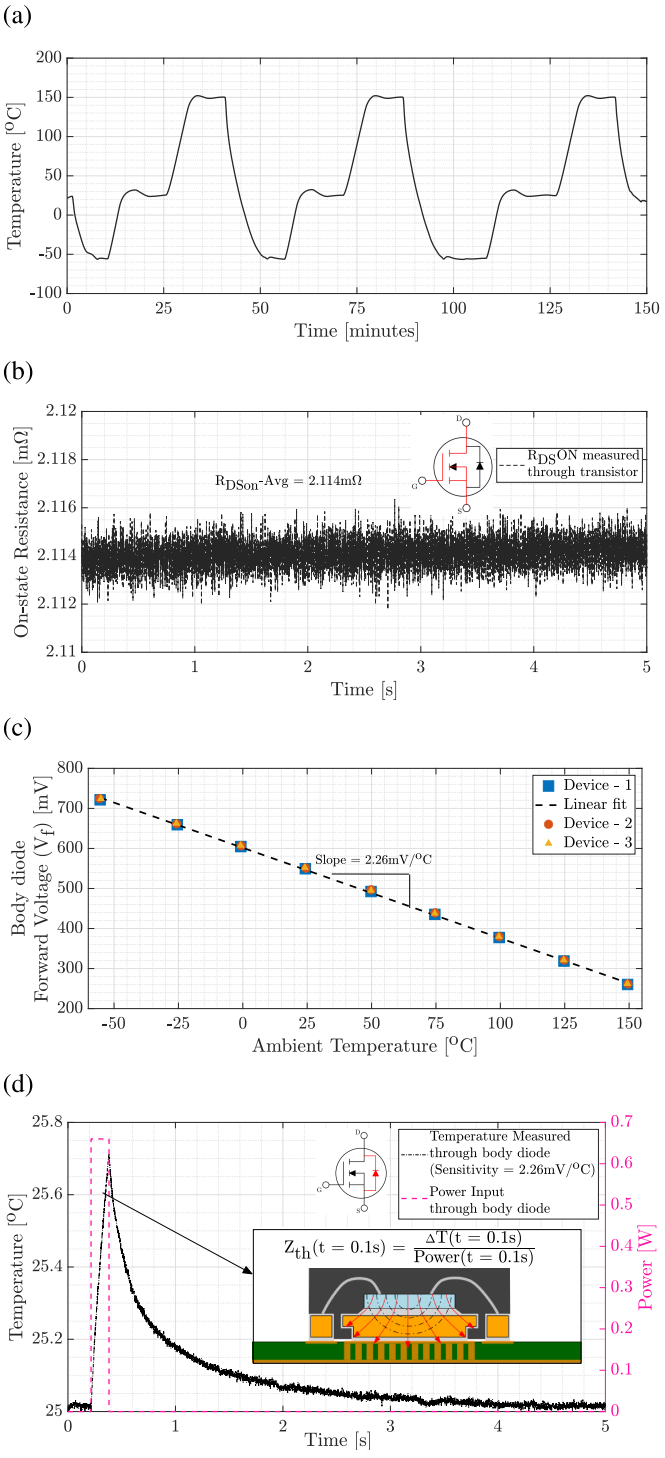

Fig. 3. (a) Thermal cycling profile. (b) R_{DSon} measured over five seconds with V_{GS} of 10 V and I_D of 1 A. (c) Calibration of body diode forward voltage (V_f) at nine different temperatures ranging from −55 °C to +150 °C on three different devices exhibiting a linear relation of 2.26 mV/ °C. (d) $Z_{\mathrm{th}}(t)$ determined based on localized heating through the body diode ($V_{\mathrm{GS}} = 0$ V and $-I_D = I_S = 1$ A). The heat flow path within 0.1 s of heating is schematically illustrated.

A brief localized heat pulse was applied to cause local temperature changes without deviating from the oven's ambient condition. Our previous work [30] determined a heating transit window of 0.1 s using a 1-D time-domain structure function. The system's thermal behavior can also be modeled in the frequency domain as explained in [36] and [37]. In [38],

a multidimensional approach was introduced for determining structure function, considering heat transfer in all directions. In this study, the transient heat pulse of 0.1 s was chosen based on our previous work. The 0.1-s heating defines a thermal resistance boundary within the package, excluding the influence of PCB materials on the measured $Z_{\text{th}}(t)$ [see Fig. 3(d)]. The solder joint interface was assumed to remain relatively stable during TMCL due to matching coefficient of thermal expansion (CTE) between the leadframe and solderable top surface of the test board. Besides, the $Z_{\text{th}}(t)$ was determined during the heating phase; estimating $Z_{\text{th}}(t)$ upon cooling down (after 0.1 s of heating) might be less sensitive since the device does not reach a steady state within 0.1 s of heating. However, the heat generated is spread across the device, and the temperature changes are averaged. Therefore, $Z_{\text{th}}(t)$ may not be influenced by localized failures originating within a small regime until sufficiently large failures occur.

Based on the aforementioned methods, the package performance was monitored as follows.

1) The electrical R_{DSon}-Avg parameter was statistically evaluated by measuring multiple samples for each material type at specific thermal cycling intervals: 0, 100, 200, 500, and 1000 cycles, all at room temperature (~25 °C).
2) The thermal impedance $Z_{\text{th}}(t = 0.1\text{ s})$ parameter was monitored online by measuring one sample per material type at 25 °C during thermal cycling.

Additionally, the online monitored samples were intermittently examined with confocal scanning acoustic microscopy (CSAM) imaging to identify degradation evolution and further cross-sectioned after 1000 cycles. The experimental findings are discussed in Section III.

III. Experimental Results

A. Prognostic Monitoring Based on Electrical Measurements

The changes in electrical R_{DSon}-Avg over TMCL were statistically analyzed using standard deviation to assess the die-attach material reliability under thermomechanical stresses. Standard deviation helps in identifying the inherent variability within the dataset, based on the dispersion of measurements around their mean value and outliers. Outliers signify sudden failures or significant deviations during TMCL. The measurements were also analyzed using Weibull probability distribution. Weibull analysis helps to understand the predictable pattern in R_{DSon}-Avg over TMCL, which is crucial for assessing material reliability. It is important to note that outliers were excluded when determining the Weibull probability distribution to prevent skewing of regression lines.

Eleven packages were tested for Material-A, ten packages for Material-B, and nine packages for Materials C and D. The arithmetic mean and standard deviation of R_{DSon}-Avg was calculated for each material type and plotted along with identified outliers in Fig. 4. A 20% deviation in R_{DSon}-Avg from the reference zero-cycle mean was considered a failure criterion. Furthermore, the Weibull probability distributions were determined for each thermal cycling interval and plotted with linear regression lines to assess whether the R_{DSon}-Avg changes conformed to the expected Weibull distribution behavior. The following conclusions can be drawn based on the results presented graphically in Fig. 4.

1) Packages with Material-A (pressure-assisted Ag-sintering with 20 MPa at 250 °C) exhibited no outliers and a steady increase in mean R_{DSon}-Avg with 6% deviation over 1000 cycles [see Fig. 4(a)]. Although the probability distribution seems to broaden over cycling, most measurements stayed around the expected Weibull behavior, with sufficient margin from the threshold, suggesting good material reliability and a predictable pattern.
2) Packages with Material-B (pressure-assisted Ag-sintering with 10 MPa at 250 °C) displayed a wider spread in R_{DSon}-Avg and a broader distribution of probabilities compared to Material-A [see Fig. 4(b)]. Besides, four outliers were identified after 500 cycles. Excluding these outliers, the remaining samples indicate <6% change in mean R_{DSon}-Avg and align closer to the Weibull prediction. However, Material-B might be less reliable than Material-A due to higher variability and outliers.
3) Packages with Material-C (pressureless Ag-sintering at 250 °C) demonstrated consistent performance without any outliers similar to Material-A [see Fig. 4(c)]. The packages demonstrated less than 2% deviation up to 500 cycles, followed by a steep increase (6.2% deviation) after 1000 cycles. The Weibull analysis indicates a similar trend, and the probability distribution centered closer to the prediction. The results suggest that Material-C exhibits good reliability with predictable behavior but may experience degradation after extended thermal cycling.
4) Packages with Material-D (pressureless resin reinforced hybrid-Ag at 200 °C) indicated the highest initial mean R_{DSon}-Avg (at zero cycles) among all materials. They also drifted 21% in mean R_{DSon}-Avg, surpassing the threshold within 500 cycles, which further escalates to 33% after 1000 cycles. Out of nine tested samples, five samples were identified as outliers, with two samples exceeding 5-mΩ resistance [see Fig. 4(d)]. Excluding these outliers, the few remaining samples are conformed around the linear regression line with a broader distribution range. Material-D indicates poor reliability due to an increase in resistance and increasing outliers.

In summary, Material-A and Material-C demonstrated consistent performance with minimal increase in R_{DSon}, without any outliers, and good alignment with the Weibull distribution. Material-B indicated acceptable performance within limits but had increasing outliers, and its Weibull suggested higher variability compared to Materials A and C. Material-D displayed reliability concerns, exceeding the threshold criterion and a substantial shift in Weibull distribution. These results suggest that packages with Material-A and Material-C perform relatively better under thermal cycling conditions compared to Material-B and Material-D.

To further differentiate the degradation behavior observed between all four die-attach materials, the transient thermal

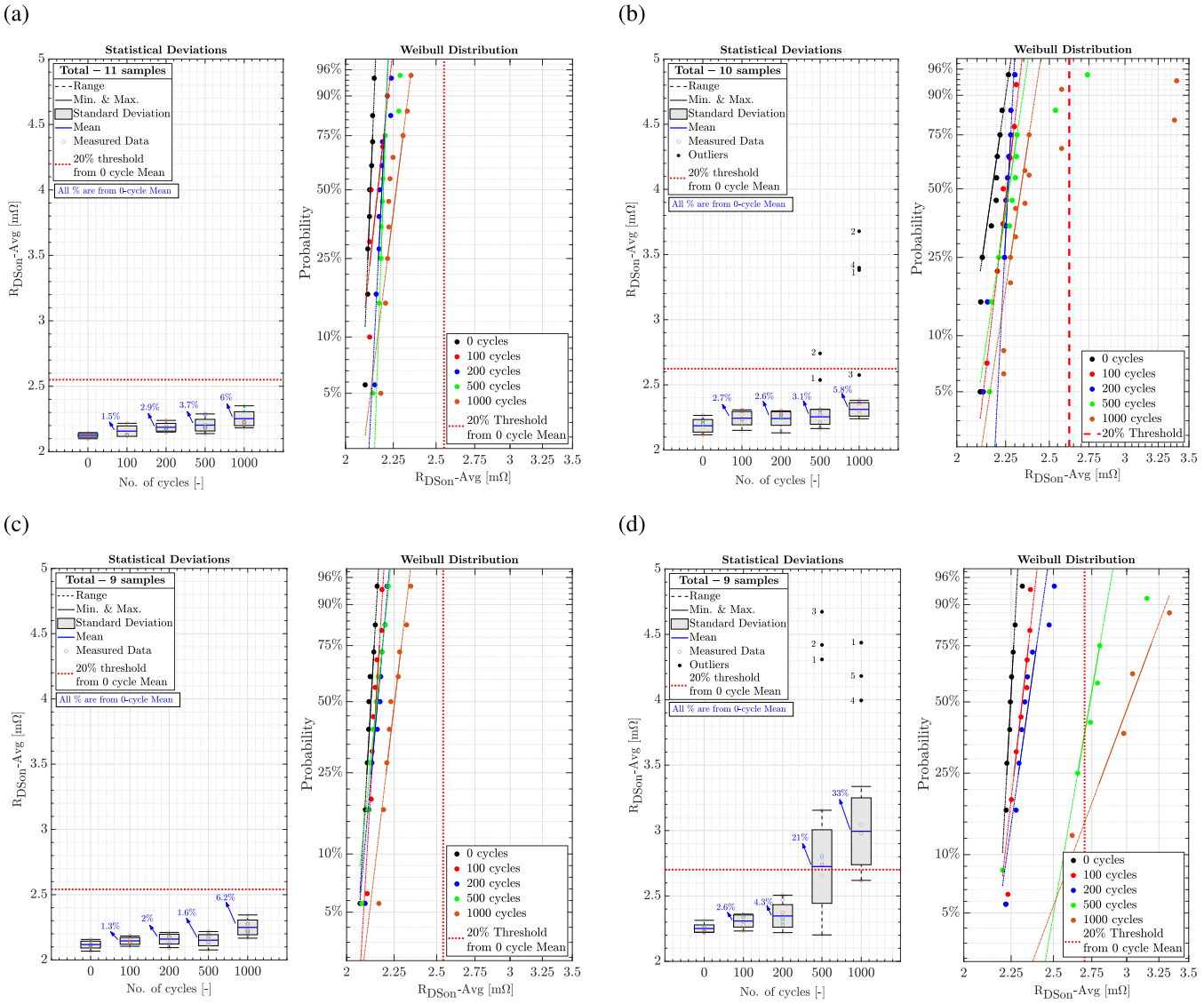

Fig. 4. Thermomechanical reliability of packages with different die-attach materials evaluated based on electrical measurements at room temperature (∼25 °C). A 20% deviation from the zero-cycle mean was considered a failure criterion. Outliers were excluded when determining the Weibull probability distribution. (a) Material-A. (b) Material-B. (c) Material-C. (d) Material-D.

impedance based on a transient pulse, $Z_{\text{th}}(t = 0.1\ \text{s})$, was monitored online, and the results are presented subsequently.

B. Prognostic Monitoring Based on Thermal Measurements

Material degradation is inevitable due to continuous thermal cycling conditions, causing reliability issues such as die-attach delamination or fractures that impede heat dissipation and thermal performance. To monitor the die-attach material degradation, the transient thermal impedance $Z_{\text{th}}(t = 0.1\ \text{s})$ was measured online during the thermal cycling test (see Fig. 5). To visually distinguish long-term trends from measurement fluctuations, simple moving averages (SMAs) over a fixed observation window (20 cycles) were determined and superimposed on the real-time measurement data in Fig. 5. The 20-cycle moving averages illustrate the measurement fluctuations and the overall degradation trend.

The thermal measurement results were further correlated with CSAM images from 0, 100, 200, 500, and 1000 thermal cycles. CSAM inspection identified two distinct failure modes (see Fig. 5): 1) delamination of epoxy molding compound and 2) delamination at the die-attach interface. Since the dominant heat flow path is through the die and die-attach, overmold delamination might not directly affect thermal measurements. However, it can strain bond wires and impact electrical resistance shown in Fig. 4, potentially explaining outliers in Materials B and D. Overmold delamination poses additional risks due to moisture ingress and package instability, potentially leading to long-term performance degradation.

The focus of this study is on the die-attach interface, which acts as a thermal transfer medium between the die and the package substrate. Delamination or failure of the die-attach layer might significantly affect the package's thermal performance. The die-attach material, sandwiched between the silicon die and the copper substrate, endures thermomechanical stresses, particularly shearing forces acting from the edges toward the center of the die. An estimate of the die-attach interface delamination from the outer edges is shown in Fig. 5. The following observations can

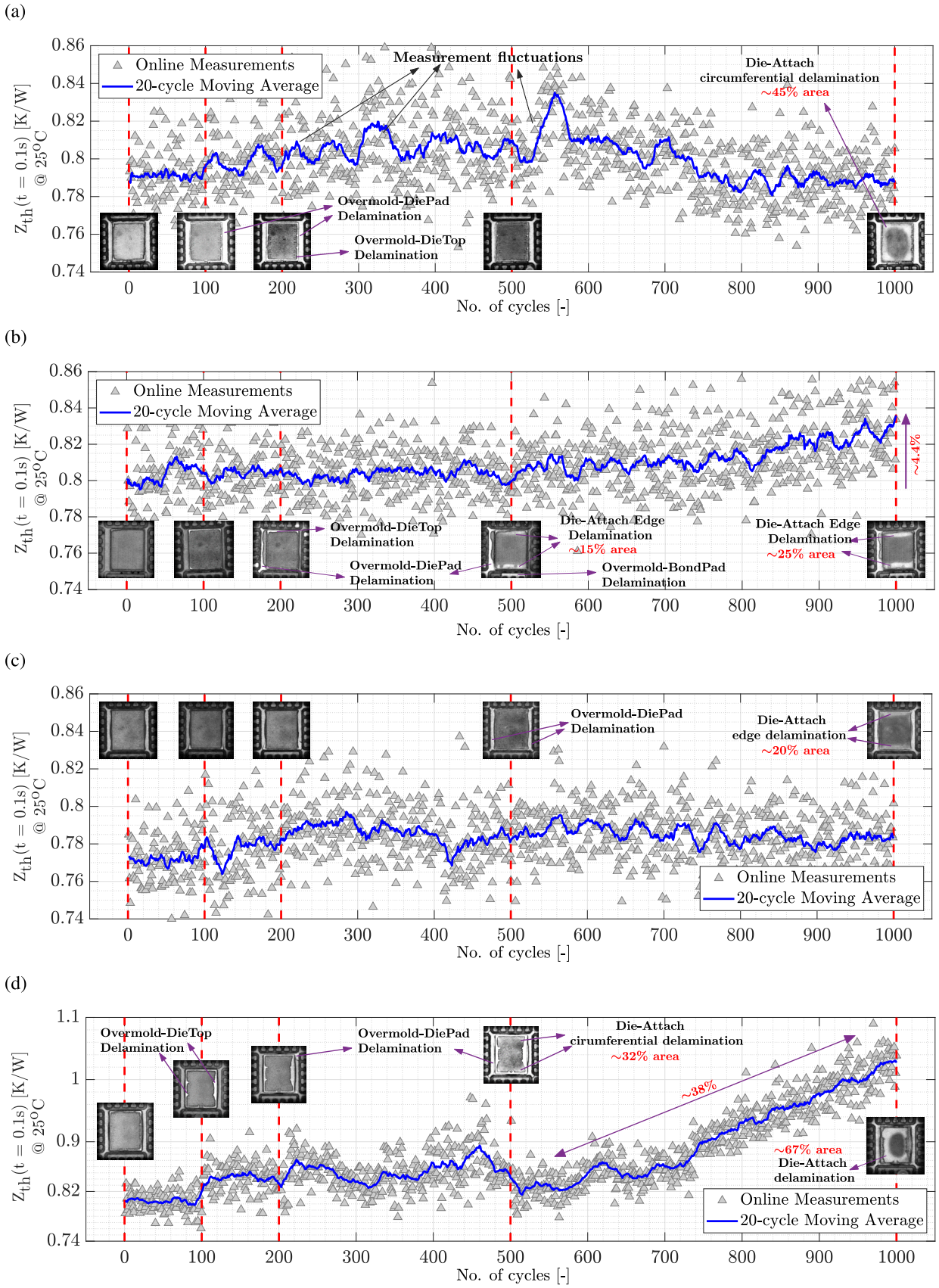

Fig. 5. Thermomechanical reliability of packages with different die-attach materials evaluated based on thermal measurements. The $Z_{th}(t = 0.1$ s) was measured at 25 °C during every thermal cycling step. Likewise, the samples were imaged using CSAM at intervals of 0, 100, 200, 500, and 1000 cycles. (a) Material-A. (b) Material-B. (c) Material-C. (d) Material-D.

be made by comparing the thermal measurements with CSAM images.

1) The package with Material-A (pressure-assisted Ag-sintering with 20 MPa at 250 °C) exhibits a fluctuating $Z_{\text{th}}(t = 0.1\text{ s})$ [see Fig. 5(a)]. These fluctuations likely originate from packaging material degradation. CSAM analysis reveals ∼45% die-attach interface delamination along the circumference, but marginal changes are observed in the measurements. This suggests that die-attach degradation along the outer edges has minimal impact on package thermal performance, possibly due to heat dissipation through the bonded area at the center.
2) The package with Material-B (pressure-assisted Ag-sintering with 10 MPa at 250 °C) exhibits stable heat transfer up to ∼500 thermal cycles and the $Z_{\text{th}}(t)$ increases moderately by ∼4.4% over 1000 cycles [see Fig. 5(b)]. CSAM analysis shows ∼15% edge delamination at 500 cycles, escalating to ∼25% after 1000 cycles. CSAM images correlated with thermal measurements seem to suggest that the dominant heat transfer path remains through the die-attach center despite edge delaminations.
3) The package with Material-C (pressureless Ag-sintering at 250 °C) exhibits a relatively lower initial $Z_{\text{th}}(t)$ at zero cycles compared to other materials although the differences are marginal [see Fig. 5(c)]. Material-C displays stable thermal performance over 1000 cycles with minimal fluctuations highlighting the material's resilience, and ∼20% edge delamination highlights the dominant heat dissipation through the center.
4) The package with Material-D (pressureless resin reinforced hybrid-Ag sintering at 200 °C) exhibits the highest initial $Z_{\text{th}}(t)$ at zero cycles with a fluctuating trend. Furthermore, Material-D shows thermal degradation, with a notable ∼38% increase in $Z_{\text{th}}(t)$ between 500 and 1000 cycles [see Fig. 5(d)]. CSAM inspection supports these findings, revealing ∼32% delamination along the circumference at 500 cycles, which escalates to ∼67% extending toward the center after 1000 cycles. This extensive delamination explains the increase in thermal impedance observed for Material-D.

All four packages were further cross-sectioned after 1000 thermal cycles and imaged using an electron microscope (see Fig. 6). Packages with pure-Ag sintering paste (Materials A–C) exhibit relatively dense sintered layers compared to the resin-filled porous interface (Material-D). Likewise, pressure-assisted sintering (Materials A and B) favors dense sintered interconnects, with Material-A exhibiting a visibly denser interface than Material-B due to increased pressure. Notably, the pressureless pure-Ag material sintered at 250 °C (Material-C) exhibits a comparatively dense sintered interconnect despite pressureless processes.

However, all four materials experienced failure closer to the die-backside metallization layer, and the severity varies across materials, with Material-D exhibiting the most deviation. The failure regions observed from the cross-sectional inspection coincide with CSAM images. Though the precise mechanism

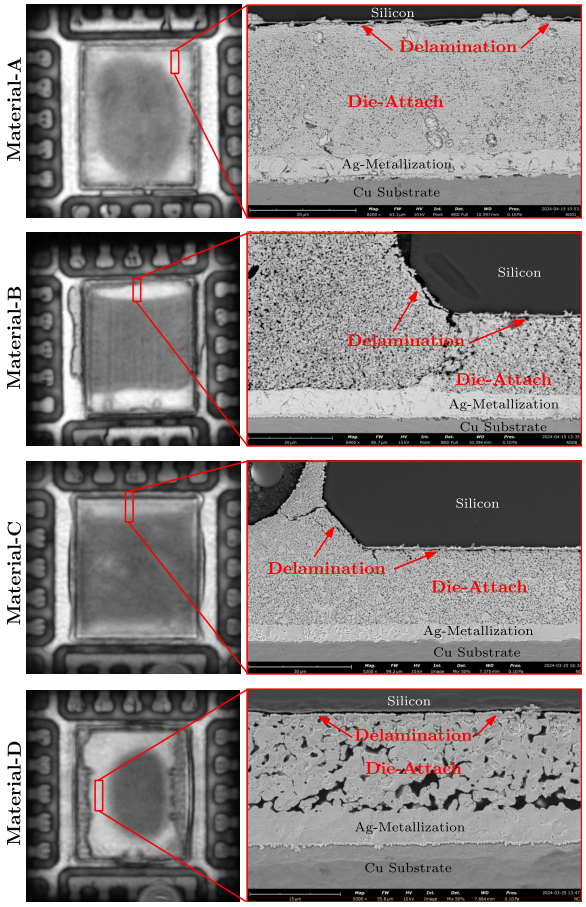

Fig. 6. Cross section of online monitored samples after 1000 cycles. The samples were polished to a desired depth and milled using a broad ion beam.

underlying the accelerated degradation of Material-D is not known, it is evident that the resin-reinforced material suffers from thermomechanical fatigue despite lower elastic modulus. Further investigations are recommended for all four materials to understand the correlation between the material microstructure and its thermomechanical performance.

In summary, the thermal measurement results, CSAM images, and cross-sectional inspection are in agreement with electrical measurement results, despite the potential influence of overmold delamination on the measured electrical R_{DSon}.

C. Discussion

The impact of die-attach material selection and their processing techniques on the thermomechanical reliability of electronic packages was investigated in this study. The experimental findings indicate a correlation between the thermomechanical reliability of the die-attach interface and the sintered interface material density. A dense sintered interconnect seems to be more resilient to thermomechanical stresses shearing from the outer edges to the center. However, further investigations are required to validate the correlation. Besides, the experimental results offer additional valuable insights.

1) *Pressureless Silver Sintering:*
   a) Pressureless Ag-sintering demonstrated consistent electrical and thermal performance, with a relatively dense interface comparable to

pressure-assisted sintering. This contradicts the assumption that pressure is typically required to achieve a dense sintered layer.

b) From a manufacturability standpoint, pressureless Ag-sintering can be advantageous by simplifying the assembly process (eliminating the need for pressure) and potentially reducing costs.

c) Pressureless Ag-sintering is a promising approach for Pb-free die-attach applications. However, not all pressureless Ag-sintering materials might exhibit similar performance. Further investigations are recommended to characterize the relationship between the material microstructure and its thermomechanical performance.

2) *Resin-Reinforced Hybrid-Silver Sintering Material:*

a) Despite resin-reinforced hybrid-Ag paste having a relatively lower modulus, they displayed degradation in this study with ∼33% drift in R_{DSon}, ∼38% increase in $Z_{\mathrm{th}}(t)$, and ∼67% interface delamination over 1000 cycles.

b) However, it is important to acknowledge that the chemical compounds used in this material are proprietary to the material supplier, and they might vary among different suppliers. Hence, further investigations are required to understand and optimize this material.

3) *Die-Attach Prognostic Monitoring:*

a) While measuring R_{DSon} and $Z_{\mathrm{th}}(t)$ that are representative parameters for monitoring the package performance signifying die-attach materials, there are limitations.

b) Despite four-point kelvin contacts, the electrical measurements might be influenced by external factors (nonuniform current spreading, gate leakage, and solder-joint degradation). Similarly, $Z_{\mathrm{th}}(t)$ can be impacted by temperature gradients within the package.

c) Future studies can explore specialized test structures to isolate the die-attach interface contribution from the R_{DSon} measurements. Likewise, $Z_{\mathrm{th}}(t)$ based on variable transit time, analyzing under frequency domain [36], [37] and incorporating multidimensional approach [38], can further improve the measurements.

IV. Conclusion

In this study, the thermomechanical reliability of PQFN packages was investigated with four distinct Ag-sintering materials:

1) (A and B) pressure-assisted Ag 20 and 10 MPa at 250 °C;
2) (C) pressureless Ag at 250 °C;
3) (D) pressureless resin-reinforced hybrid-Ag at 200 °C.

The lifetime reliability of these die-attach materials was assessed under thermal cycling conditions by monitoring the drift in electrical ON-state resistance R_{DSon}, and changes in transient thermal impedance $Z_{\mathrm{th}}(t = 0.1\ \mathrm{s})$. The measurement results were further validated with CSAM imaging and cross-sectional inspection.

The pressureless Ag-sintered (Material-C) demonstrated consistent electrical and thermal performances with sintered interconnect density comparable to pressure-assisted sintering materials. Whereas the pressureless resin-reinforced hybrid-Ag sintered at a lower temperature (Material-D) indicated reliability concerns with ∼33% increase in R_{DSon}, ∼38% in $Z_{\mathrm{th}}(t = 0.1\ \mathrm{s})$, and ∼67% delamination over 1000 thermal cycles. The experimental findings suggest a correlation between the die-attach material density and their thermomechanical reliability, which requires further experimental verification.

This comprehensive study underscores the importance of die-attach material selection and recommends careful consideration of thermomechanical properties during package design. Furthermore, such efforts in implementing prognostic monitoring strategies are crucial in understanding performance degradation to create better awareness, make informed decisions, and schedule preemptive maintenance.

Acknowledgment

The authors extend their gratitude to fellow researchers from Delft University of Technology (TUD) and the Chip Integration Technology Center (CITC) for their valuable support in this comprehensive test work. Thanks to Dave Reijs from CITC for his valuable support with the package assembly process and to Noud Schoenmakers from CITC for his support with broad-ion beam milling.

References

[1] H. Wang et al., "Transitioning to physics-of-failure as a reliability driver in power electronics," *IEEE J. Emerg. Sel. Topics Power Electron.*, vol. 2, no. 1, pp. 97–114, Mar. 2014, doi: 10.1109/JESTPE.2013.2290282.

[2] H. Wang, M. Liserre, and F. Blaabjerg, "Toward reliable power electronics: Challenges, design tools, and opportunities," *IEEE Ind. Electron. Mag.*, vol. 7, no. 2, pp. 17–26, Jun. 2013, doi: 10.1109/MIE.2013.2252958.

[3] H. Wang and F. Blaabjerg, "Power electronics reliability: State of the art and outlook," *IEEE J. Emerg. Sel. Topics Power Electron.*, vol. 9, no. 6, pp. 6476–6493, Dec. 2021, doi: 10.1109/JESTPE.2020.3037161.

[4] H. A. Martin, E. C. P. Smits, R. H. Poelma, W. D. van Driel, and G. Q. Zhang, "An outlook on power electronics reliability and reliability monitoring," in *Recent Advances in Microelectronics Reliability*, W. D. van Driel, K. Pressel, and M. Soyturk, Eds., Eds., Cham, Switzerland: Springer, 2024, pp. 251–282, doi: 10.1007/978-3-031-59361-1_10.

[5] K. S. Siow, "Die-attach materials for high temperature applications in microelectronics packaging," in *Materials, Processes, Equipment, and Reliability*. Springer, 2019.

[6] M. Ciappa, "Selected failure mechanisms of modern power modules," *Microelectron. Rel.*, vol. 42, no. 4, pp. 653–667, 2002, doi: 10.1016/S0026-2714(02)00042-2. [Online]. Available: https://www.sciencedirect.com/science/article/pii/S0026271402000422

[7] Chemical Safety and Health Unit (CHE) and World Health Organization. (2018). *The Public Health Impact of Chemicals: Knowns and Unknowns*. [Online]. Available: https://www.who.int/publications/i/item/WHO-FWC-PHE-EPE-16-01

[8] *The European Semiconductor Industry and PFAS—Summary Paper*, Eur. Semiconductor Ind. Assoc., Brussel, Belgium, 2023, pp. 1–4.

[9] A. Hussain, H. L. Lee, and S. J. Moon, "Sintering of silver nanoparticle structures and the pursuit of minimum resistivity," *Mater. Today Commun.*, vol. 34, Mar. 2023, Art. no. 105159, doi: 10.1016/j.mtcomm.2022.105159.

[10] H. A. Martin, S. Libon, E. C. P. Smits, R. H. Poelma, W. D. van Driel, and G. Zhang, "Thermal characterization methodology for thin bond-line interfaces with high conductive materials," *Thermal Sci. Eng. Prog.*, vol. 53, 2024, Art. no. 102754, doi: 10.1016/j.tsep.2024.102754. [Online]. Available: https://www.sciencedirect.com/science/article/pii/S245190492400372X

[11] G. Chen, Y. Cao, Y. Mei, D. Han, G.-Q. Lu, and X. Chen, "Pressure-assisted low-temperature sintering of nanosilver paste for 5×5-mm^2 chip attachment," *IEEE Trans. Compon., Packag., Manuf. Technol.*, vol. 2, no. 11, pp. 1759–1767, Nov. 2012, doi: 10.1109/TCPMT.2012.2214481.

[12] J. Fan, D. Xu, H. Zhang, C. Qian, X. Fan, and G. Zhang, "Experimental investigation on the sintering kinetics of nanosilver particles used in high-power electronic packaging," *IEEE Trans. Compon., Packag., Manuf. Technol.*, vol. 10, no. 7, pp. 1101–1109, Jul. 2020, doi: 10.1109/TCPMT.2020.2995634.

[13] W. Liu, C. Wang, C. Wang, X. Jiang, and X. Huang, "Laser sintering of nano-Ag particle paste for high-temperature electronics assembly," *IEEE Trans. Compon., Packag., Manuf. Technol.*, vol. 7, no. 7, pp. 1050–1057, Jul. 2017, doi: 10.1109/TCPMT.2017.2696967.

[14] P. Lu et al., "Ultrasonic-assisted micro-silver paste sintering for flip-chip bonding," *IEEE Trans. Compon., Packag., Manuf. Technol.*, vol. 12, no. 8, pp. 1395–1400, Aug. 2022, doi: 10.1109/TCPMT.2022.3194644.

[15] S. K. Bhogaraju, A. Hanß, M. Schmid, G. Elger, and F. Conti, "Evaluation of silver and copper sintering of first level interconnects for high power LEDs," in *Proc. 7th Electron. Syst.-Integr. Technol. Conf. (ESTC)*, Sep. 2018, pp. 1–8, doi: 10.1109/ESTC.2018.8546499.

[16] H. Zheng, D. Berry, K. D. T. Ngo, and G.-Q. Lu, "Chip-bonding on copper by pressureless sintering of nanosilver paste under controlled atmosphere," *IEEE Trans. Compon., Packag., Manuf. Technol.*, vol. 4, no. 3, pp. 377–384, Mar. 2014, doi: 10.1109/TCPMT.2013.2296882.

[17] J. Kahler, N. Heuck, A. Wagner, A. Stranz, E. Peiner, and A. Waag, "Sintering of copper particles for die attach," *IEEE Trans. Compon., Packag., Manuf. Technol.*, vol. 2, no. 10, pp. 1587–1591, Oct. 2012, doi: 10.1109/TCPMT.2012.2201940.

[18] B. Zhang, X. Lu, H. Ma, D. Wang, and Y.-H. Mei, "Development of silver paste with high sintering driving force for reliable packaging of power electronics," *IEEE Trans. Compon., Packag., Manuf. Technol.*, vol. 14, no. 1, pp. 10–17, Jan. 2024, doi: 10.1109/TCPMT.2023.3347250.

[19] S. Krishnan, A. S. M. A. Haseeb, and M. R. Johan, "Preparation and low-temperature sintering of Cu nanoparticles for high-power devices," *IEEE Trans. Compon., Packag., Manuf. Technol.*, vol. 2, no. 4, pp. 587–592, Apr. 2012, doi: 10.1109/TCPMT.2012.2189208.

[20] X. Liu et al., "Microstructural evolution, fracture behavior and bonding mechanisms study of copper sintering on bare DBC substrate for SiC power electronics packaging," *J. Mater. Res. Technol.*, vol. 19, pp. 1407–1421, Jul. 2022, doi: 10.1016/j.jmrt.2022.05.122.

[21] S. Chen, Y.-H. Mei, M. Wang, X. Li, and G.-Q. Lu, "Large-area bonding by sintering of a resin-free nanosilver paste at ultralow temperature of 180 °C," *IEEE Trans. Compon., Packag., Manuf. Technol.*, vol. 12, no. 4, pp. 707–710, Apr. 2022, doi: 10.1109/TCPMT.2022.3159033.

[22] N. Mizumura and K. Sasaki, "Development of low-temperature sintered nano-silver pastes using MO technology and resin reinforcing technology," in *Proc. Int. Conf. Electron. Packag. (ICEP)*, Apr. 2014, pp. 526–531, doi: 10.1109/ICEP.2014.6826735.

[23] X. Hu et al., "Microstructure analysis based on 3D reconstruction model and transient thermal impedance measurement of resin-reinforced sintered Ag layer for high power RF device," in *Proc. 24th Int. Conf. Thermal, Mech. Multi-Phys. Simulation Exp. Microelectron. Microsyst. (EuroSimE)*, Apr. 2023, pp. 1–7, doi: 10.1109/EuroSimE56861.2023.10100799.

[24] M. Schaal, M. Klingler, and B. Wunderle, "Silver sintering in power electronics: The state of the art in material characterization and reliability testing," in *Proc. 7th Electron. Syst.-Integr. Technol. Conf. (ESTC)*, Sep. 2018, pp. 1–18, doi: 10.1109/ESTC.2018.8546498.

[25] W. Liu et al., "Recent progress in rapid sintering of nanosilver for electronics applications," *Micromachines*, vol. 9, no. 7, p. 346, Jul. 2018, doi: 10.3390/mi9070346.

[26] D. Leslie and A. Dasgupta, "Viscoplastic properties of pressure-less sintered silver materials using indentation," in *Proc. 17th Int. Conf. Thermal, Mech. Multi-Phys. Simulation Exp. Microelectron. Microsyst. (EuroSimE)*, Apr. 2016, pp. 1–5, doi: 10.1109/EuroSimE.2016.7463371.

[27] D. Leslie, A. Dasgupta, and C. Morillo, "Viscoplastic properties of pressure-less sintered silver materials using indentation," *Microelectron. Rel.*, vol. 74, pp. 121–130, Jul. 2017, doi: 10.1016/j.microrel.2017.04.009.

[28] M. A. Gharaibeh and J. Wilde, "Research on the creep response of lead-free die attachments in power electronics," *Int. J. Struct. Integrity*, vol. 15, no. 4, pp. 702–716, Aug. 2024, doi: 10.1108/ijsi-01-2024-0005.

[29] M. A. Gharaibeh and J. Wilde, "Numerical evaluation of sintered silver die attachments based on different material parameters and creep constitutive models," *IEEE Trans. Compon., Packag., Manuf. Technol.*, vol. 13, no. 8, pp. 1187–1201, Aug. 2023, doi: 10.1109/TCPMT.2023.3298744.

[30] H. A. Martin, E. C. P. Smits, R. H. Poelma, W. D. van Driel, and G. Zhang, "Online condition monitoring methodology for power electronics package reliability assessment," *IEEE Trans. Power Electron.*, vol. 39, no. 4, pp. 4725–4734, Apr. 2024, doi: 10.1109/TPEL.2024.3352747.

[31] F. Hosseinabadi, S. Chakraborty, S. K. Bhoi, G. Prochart, D. Hrvanovic, and O. Hegazy, "A comprehensive overview of reliability assessment strategies and testing of power electronics converters," *IEEE Open J. Power Electron.*, vol. 5, pp. 473–512, 2024, doi: 10.1109/OJPEL.2024.3379294.

[32] D. Kim et al., "Online thermal resistance and reliability characteristic monitoring of power modules with Ag sinter joining and Pb, Pb-free solders during power cycling test by SiC TEG chip," *IEEE Trans. Power Electron.*, vol. 36, no. 5, pp. 4977–4990, May 2021, doi: 10.1109/TPEL.2020.3031670.

[33] A. A. Wereszczak, D. J. Vuono, H. Wang, M. K. Ferber, and Z. Liang. (2012). *Properties of Bulk Sintered Silver As a Function of Porosity*. [Online]. Available: https://api.semanticscholar.org/CorpusID:135565266

[34] Z. Hu et al., "Degradation in electrothermal characteristics and failure mechanism of SiC JBS with different die attach materials under 300 °C power cycle stress," *IEEE J. Emerg. Sel. Topics Power Electron.*, vol. 12, no. 4, pp. 3619–3628, Aug. 2024, doi: 10.1109/JESTPE.2024.3380026.

[35] V. d'Alessandro et al., "A critical review of techniques for the experimental extraction of the thermal resistance of bipolar transistors from DC measurements—Part I: Thermometer-based approaches," *Electronics*, vol. 12, no. 16, p. 3471, Aug. 2023, doi: 10.3390/electronics12163471.

[36] K. Ma, N. He, M. Liserre, and F. Blaabjerg, "Frequency-domain thermal modeling and characterization of power semiconductor devices," *IEEE Trans. Power Electron.*, vol. 31, no. 10, pp. 7183–7193, Oct. 2016, doi: 10.1109/TPEL.2015.2509506.

[37] C. Scognamillo, S. Fregonese, T. Zimmer, V. d'Alessandro, and A. P. Catalano, "A technique for the in-situ experimental extraction of the thermal impedance of power devices," *IEEE Trans. Power Electron.*, vol. 37, no. 10, pp. 11511–11515, Oct. 2022, doi: 10.1109/TPEL.2022.3174617.

[38] L. Codecasa, V. d'Alessandro, A. P. Catalano, C. Scognamillo, and D. D'Amore, "Structure curve representation of dynamic thermal multi-ports," in *Proc. 29th Int. Workshop Thermal Investigations ICs Syst. (THERMINIC)*, Sep. 2023, pp. 1–7, doi: 10.1109/therminic60375.2023.10325682.